

Optimization of wide frequency range 6H-SiC MEMS chips for a fiber optic Fabry-Perot accelerometer

Mariano Mahissi(马依思 马里亚诺), Xinli Ma(马新莉), Weiming Cai(蔡卫明), Xianmin Zhang(章献民), and Michel Dossou(多苏 米歇尔)

Citation: Chin. Phys. B, 2025, 34 (**7**): 074203. DOI: 10.1088/1674-1056/adc18e
http://cpb.iphy.ac.cn; http://iopscience.iop.org/cpb

What follows is a list of articles you may be interested in

Resolving gravitational redshift with sub-millimeter height differences using spin-squeezed optical clocks

Deshui Yu(于得水), Jia Zhang(张佳), Shougang Zhang(张首刚), Tiantian Shi(史田田), and Jingbiao Chen(陈景标)
Chin. Phys. B, 2025, 34 (**5**): 054208. DOI: 10.1088/1674-1056/adca1d

Electromagnetically-induced-absorption-like ground state cooling in a hybrid optomechanical system

Yaoyong Dong(董耀勇), Xuejun Zheng(郑学军), Denglong Wang(王登龙), and Peng Zhao(赵鹏)
Chin. Phys. B, 2025, 34 (**4**): 044203. DOI: 10.1088/1674-1056/adb260

Vector fiber Bragg gratings accelerometer based on silicone compliant cylinder for low frequency vibration monitoring

Wenyu Hu(胡文玉), Zhuo Chen(陈卓), Jiangshan You(尤江山), Ruohui Wang(王若晖), Rui Zhou(周锐), and Xueguang Qiao(乔学光)
Chin. Phys. B, 2023, 32 (**11**): 114201. DOI: 10.1088/1674-1056/acec43

Design of three-dimensional imaging lidar optical system for large field of view scanning

Qing-Yan Li(李青岩), Yu Zhang(张雨), Shi-Yu Yan(闫诗雨),Bin Zhang(张斌), and Chun-Hui Wang(王春晖)
Chin. Phys. B, 2022, 31 (**7**): 074201. DOI: 10.1088/1674-1056/ac4a67

Dynamic measurement of beam divergence angle of different fields of view of scanning lidar

Qing-Yan Li(李青岩), Shi-Yu Yan(闫诗雨), Bin Zhang(张斌), and Chun-Hui Wang(王春晖)
Chin. Phys. B, 2021, 30 (**2**): 024205. DOI: 10.1088/1674-1056/abc155

Optimization of wide frequency range 6H-SiC MEMS chips for a fiber optic Fabry–Perot accelerometer

Mariano Mahissi(马依思·马里亚诺)[1,2], Xinli Ma(马新莉)[2,†], Weiming Cai(蔡卫明)[2,‡], Xianmin Zhang(章献民)[1], and Michel Dossou(多苏·米歇尔)[3]

[1] *College of Information Science and Electronic Engineering, Zhejiang University, Hangzhou* 310027, *China*
[2] *School of Information Science and Engineering, Ningbo Tech University, Ningbo* 315100, *China*
[3] *Research Unit in Photonics and Wireless Communications, LETIA/EPAC, University of Abomey-Calavi,* 01 *BP* 526 *Abomey-Calavi, Benin*

(Received 17 December 2024; revised manuscript received 4 March 2025; accepted manuscript online 18 March 2025)

Vibration detection using sensors with both wide working frequency range, good sensitivity, and other good performances is a topic of great interest in fields such as inertial navigation, deep-sea fishing boat engines condition monitoring, seismic monitoring, attitude, and heading reference system, *etc*. This paper investigates two 6H-SIC MEMS diaphragms, one triangular and the other square, used in a fiber optic Fabry–Perot (FP) accelerometer in an experimental scenario. The triangular chip shows a wide working frequency range of 630 Hz–5300 Hz, a natural frequency of 44.3 kHz, and a mechanical sensitivity of 0.154 nm/g. An optimal structure of the square chip used in a probe such as a fiber optic FP accelerometer also shows a wide working frequency range of 120 Hz–2300 Hz; a good sensitivity of 31.5 mV/g, a resonance frequency of 7873 Hz, an accuracy of 0.96% F.S., a frequency measurement error of 1.15%, and an excellent linearity of 0.9995.

Keywords: triangular chip, accelerometer, MEMS, working frequency range, optical fiber

PACS: 42.50.–p, 62.23.–c, 61.46.–w, 42.62.Eh

DOI: 10.1088/1674-1056/adc18e **CSTR:** 32038.14.CPB.adc18e

1. Introduction

Research into accelerometers based on microelectromechanical system (MEMS) technology is a topic of great interest, as this technology is widely used in fields such as mechanics, civil aviation, high-precision seismic measurement, marine navigation, earthquake monitoring, etc.[1–3] MEMS are increasingly combined with optical fiber (OF) sensing technology to design higher-performance MEMS based OF accelerometers (MEMS–OFT).[4–7] MEMS–OFT accelerometers are mostly composed of a sensitive diaphragm, OF, and a Fabry–Perot (FP) cavity. They have attracted the attention of many researchers due to their miniaturization, high temperature operation up to 1200 °C, integration, anti-electromagnetic interference, corrosion resistance, etc.[8]

In recent years, research on MEMS–OFT accelerometers has focused on improving the performance by adopting different structures and/or demodulation methods.[9] Accelerometer structures have evolved from macro to MEMS and integrated structures.[10–12] New chip materials, new shapes of diaphragm cantilever beams, and other tricks have been used and reported to improve these sensors' performance. Li *et al*.[13] proposed an optomechanical accelerometer based on MEMS. The BK7 optical glass chip has a square shape, its central mass is connected to the frame by four simple beams, which are in turn connected to a complex spring structure. The accelerometer has a theoretical sensitivity of 893.23 μm/g, a small natural frequency of 16.67 Hz, and a very narrow working frequency range (WFR). The accelerometer has a very high resolution of 2 ng/$\sqrt{\text{Hz}}$ from 2 Hz to 7 Hz. Zhao *et al*.[5] investigated an MEMS-based FP accelerometer consisting of a square-shaped sensing chip and two G-shaped mass-spring structures. The sensing chip has a narrow WFR of about 40 Hz–60 Hz, a low resonance frequency of 89 Hz, a good acceleration measurement linearity of 0.99042, and a high sensitivity and resolution of 183.793 V/g and 300 ng, respectively. Chen *et al*.[14] studied a circular-shaped aluminum nitride-based lead-free piezoelectric MEMS accelerometer with ring beams. The diaphragm has a relatively low sensitivity of 1.49 mV, a resonant frequency of 7200 Hz, a wide WFR of about 1 Hz–5000 Hz, and a low operating temperature of 100 °C. Yang *et al*.[15] proposed a MEMS (built on a cavity SOI substrate) accelerometer with polygonal topology with six trapezoidal beams supported between the frame and the central support column. The beams also constitute the proof mass (PM) for vibration. The sensor has a WFR of 200 Hz–1500 Hz, a high natural frequency of 98000 Hz, and a low sensitivity of 1.533 mV/g. The mentioned works have improved the detection performance of chips through their shapes and different cantilever beam topologies. Chips with a square shape have several beams, each with a relatively long length. As for performance, these chips do not have a wide enough WFR and they mostly have a small natural frequency, but they have good

†Corresponding author. E-mail: maxinli@tju.edu.cn
‡Corresponding author. E-mail: caiwm@nit.zju.edu.cn

© 2025 Chinese Physical Society and IOP Publishing Ltd. All rights, including for text and data mining, AI training, and similar technologies, are reserved.

sensitivity. While other chips with other shapes mostly have a very wide WFR, a very high natural frequency, but on the other hand a relatively low sensitivity. Some aspects such as the shape or chip structural dimensions can be further optimized in order to have both a wide WFR, a high natural frequency, good sensitivity, and many other good performances.

In this paper, we designed and simulated by finite elements analysis (FEA) a triangular chip and a wide frequency range square diaphragm (WFRSD). Unlike other diaphragms, the proposed ones have the particularity of presenting a good result on all the investigated performances. The triangular chip theoretical performances show that this proposed shape has a wide WFR and at the same time a good mechanical sensitivity. Based on an optimal dimensioning, the experimental results of the WFRSD used as a fiber optic FP accelerometer show that the chip presents a wide WFR of 120 Hz–2300 Hz, a natural frequency of 7873 Hz and other good performances.

2. Diaphragms vibration principle

The mechanical system of a typical acceleration sensor is usually composed of a damped oscillators system.[16] Subjected to an external acceleration excitation, its PM acquires the same vibration as that of the exciting acceleration. Thus, the measurand can be obtained by evaluating the PM displacement.

Considering that the spring support and the mass absolute displacements are respectively x_e and x_r (see Fig. 1(a)); the sensor sensitivity being strictly linked to the mass block relative displacement with respect to that of the support, the fundamental principle of dynamics allows to write the mechanical system equation as follows:

$$z = m\frac{\mathrm{d}^2(x_r - x_e)}{\mathrm{d}t^2} + \delta\frac{\mathrm{d}(x_r - x_e)}{\mathrm{d}t} + \gamma(x_r - x_e), \tag{1}$$

where $-\delta(\mathrm{d}(x_r - x_e)/\mathrm{d}t)$ is the damping force, $-\gamma(x_r - x_e)$ is the restoring force, z is the representative function of an external force, δ and γ are the damping coefficient and the system's stiffness, respectively.

Equation (2) is the transfer function obtained from the transform of Eq. (1). By setting $\varpi = w/w_0$, we have after transformation, the system frequency response function (Eq. (3)) from the transfer function, and we deduce the amplitude–frequency function (Eq. (4)). The damped system phase response subjected to a sinusoidal force is obtained from the phase frequency function (Eq. (5)).

$$P(\upsilon) = \gamma\left[1 + (\upsilon^2/w_0^2) + (2\varsigma\upsilon/w_0)\right]^{-1}, \tag{2}$$

$$P(\mathrm{i}w) = -\gamma\left[\varpi^2 - 2\varsigma\varpi\mathrm{i} - 1\right]^{-1}, \tag{3}$$

$$|P(\mathrm{i}w)| = \gamma\left[(\varpi^2 - 1)^2 + (2\varsigma\varpi)^2\right]^{-1/2}, \tag{4}$$

$$\phi = -\arctan\left(\frac{2\varsigma\varpi}{1-\varpi^2}\right), \tag{5}$$

where $w_o = \sqrt{\gamma/m}$ is the natural angular frequency of the system, and $\varsigma = 1/2\sqrt{\delta/m}$ the damping ratio.

The damped system's amplitude–frequency curve subjected to a sinusoidal force is obtained from the amplitude–frequency function as shown in Fig. 1(b). The degree of deviation is related to the damping and is also characterized by the sensor amplitude error. As the damping ratio increases, the curve becomes flatter and flatter, indicating that the sensor's amplitude error becomes smaller, while the response band becomes wider. For undamped systems $\varsigma = 0$, critically damped systems $\varsigma = 0.707$, and overdamped systems $\varsigma > 1$. When the damping ratio is 0.6–0.7, the sensor's amplitude error is relatively small, and the response working band is wider, but the sensor sensitivity is greatly reduced. Since the damping ratio and intrinsic frequency are both related to the sensor structure, in the process of sensor designing, its structure should be optimized to reduce the amplitude error, and then increase the operating frequency and control its sensitivity in the application range.

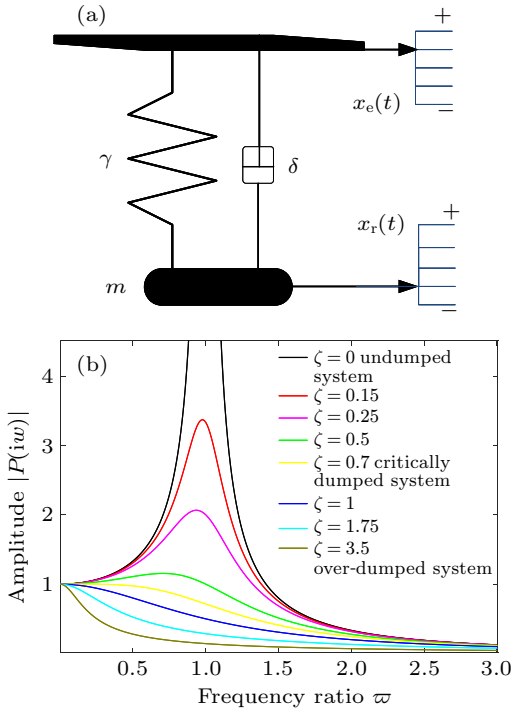


Fig. 1. (a) Acceleration sensor mechanical model, (b) graph for the amplitude–frequency characteristic of the mechanic system.

3. Chips design, simulation, and preparation

Ansys finite element analysis (FEA) software is used to simulate the vibration modes of the triangular diaphragm mass-spring structure and WFRSD to find their theoretical performances. The performance study is carried out by keeping the material properties the same, and the chip side and thickness are set to $c = 14.5$ mm and $e = 0.3$ mm, respectively. The base material used for the sensing elements is 6H-SiC. The density, Young's modulus, and Poisson's ratio are set to 3.21 g/cm^3, 450 GPa, and 0.142, respectively. The adopted

return-shaped cantilever structure functions as a damped oscillator system. Modal, harmonic response and static structural studies are investigated under the same conditions.

3.1. I-shaped cantilever beams diaphragm

The triangular chip is characterized by its three I-shaped beams, as shown in Fig. 2(a). It mainly comprises a PM (in the shape of an irregular hexagon) arranged in the chip's central part supported by three cantilever beams connected to the PM's three short sides. The PM is arranged so that the structure has the axis passing through the center as the symmetry axis to ensure that the displacement of each point of the PM is equal.

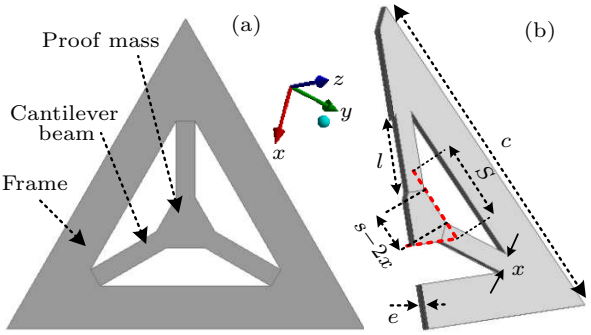


Fig. 2. Triangular MEMS chip model: (a) schematic diagram, (b) chip plan section and sizing.

The diaphragm is designed to support a range of acceleration measurements up to 20 g, a WFR between 500 Hz–5000 Hz, and a natural frequency above 40 kHz.

Considering a mechanical system of mass m, elastic coefficient k, and natural frequency f_{I}, the optimal dimensions of the triangular model are obtained by relation (6) based on the initial requirements.

$$f_{\mathrm{I}} = \frac{e}{\pi}\sqrt{\frac{\varepsilon x E}{(s^2+3x^2)\rho l^3}}, \tag{6}$$

where $k = \varepsilon x E e^3/l^3$ and $m = \rho e\frac{\sqrt{3}}{4}\left(s^2-3x^2\right)$, are the elastic coefficient and the PM's mass, respectively; ρ, E, x, e, l, s, and ε, are the material's density, material Young's modulus, elastic beam width, beam thickness, beam length, triangle's side in which the PM is inscribed, and the chip structure design constant, respectively.

Thus, the triangular model has a PM's short side length and long side of $x = 0.8$ mm and $s - 2x = 2.4$ mm, respectively (as shown in Fig. 2(b)); beam thickness $e = 0.3$ mm, chip side $c = 14.5$ mm, and beam length $l = 3.184$ mm. Figures 3(a)–3(d) displays the diaphragm's first four orders of vibration modes following a 20 g vertical acceleration at the PM center.

As shown in Fig. 3(a), the fundamental mode has a natural frequency of 44.73 kHz, the PM oscillates without torsion along Z direction. It is a translational motion oriented vertically normal to the beams plane. The beam ends in contact with the PM follow the PM motion while those in contact with the frame are fixed. The distribution of deformation energy is mainly concentrated at the PM center. With a frequency of 126.27 kHz, TBM (two-beams motion) mode is a combination of rotational and torsional motion of two beams (active beams) with the PM center almost immobile as shown in Fig. 3(b). Active beams drive the involved PM ends in their motion. The deformation has its maximum value mainly in the active beams. Unlike TBM mode, OBM (one beam motion) mode has the maximum energy in only its active beam as can be seen in Fig. 3(c). Its natural frequency is 126.32 kHz. With its center of mass almost immobile, the active beam drives one side of the PM in a combination of rotational and torsional motion. The frequency of AB (all beams) mode is 258.05 kHz (Fig. 3(d)), its deformation energy is distributed in all three beams. Beams perform a torsional motion and drive the PM contact sides. With very low deformation energy distribution in the PM's center, it remained almost immobile to the beams motion. From the analysis of four modes, it appears that only the fundamental mode allows a translational motion without torsion of the PM. Therefore, this mode is best suited for vibration sensing.

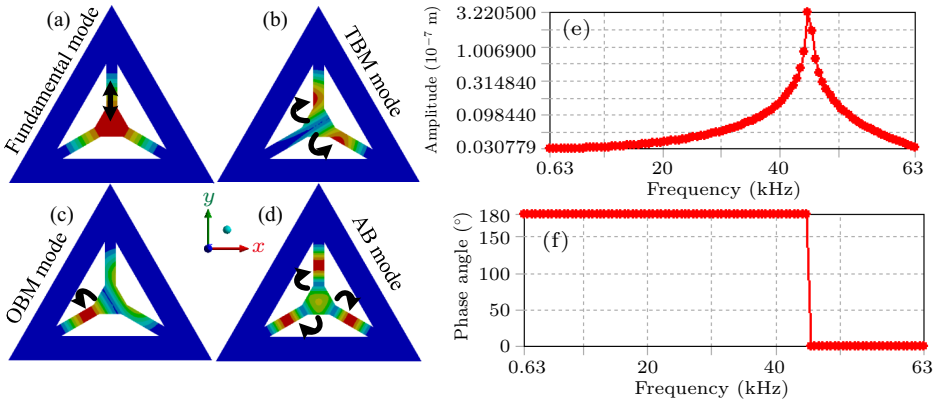


Fig. 3. FEA eigenmode simulation of triangular diaphragms and theorical characteristics: (a) fundamental mode, (b) TBM mode, (c) OBM mode, (d) AB mode, (e) amplitude–frequency characteristic, (f) phase–frequency characteristic.

The triangular chip's theoretical amplitude–frequency and phase–frequency characteristic curves are shown in Figs. 3(e) and 3(f), respectively. Both curves are horizontal between 630 Hz and 5.3 kHz, which indicates the accelerometer WFR. The amplitude–frequency curve shows a progressive rise until reaching its resonance frequency $f = 44.73$ kHz. At f, the phase shows a 180° drop to 0° characterizing the resonance state. For 2 g and 20 g excitations, we have a total deformation of 0.31 nm and 3.08 nm, respectively; which allows to evaluate the triangular chip mechanical sensitivity at 0.154 nm/g.

With the results obtained from the triangular chip theoretical study, we conclude that its theoretical performances are fully in line with the initial requirements for the model optimization.

3.2. L-shaped cantilever beams diaphragm

As can be seen from the cross section in Fig. 4(a), the square-shaped diaphragm and L-shaped beams designed in this part has a symmetrical structure at its center to ensure that the displacement of each point of the PM is equal. It is designed to have a flat frequency range of 100 Hz–2500 Hz, a resonant frequency of over 7 kHz, and to support an acceleration measurement range of 20 g.

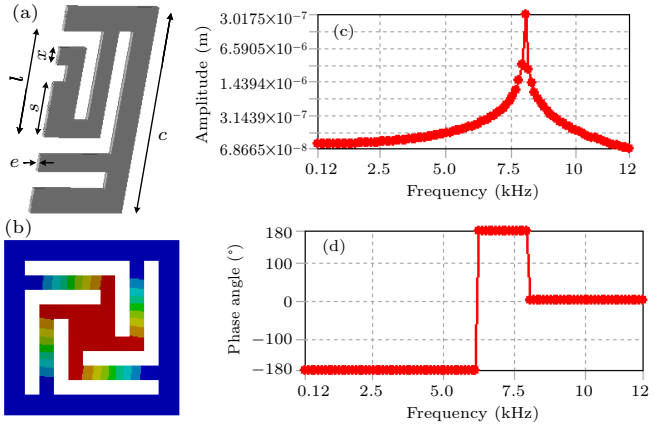


Fig. 4. Simulation results of the WFRSD designed: (a) chip cross section and sizing, (b) fundamental mode of vibration, (c) amplitude–frequency characteristic, (d) phase–frequency characteristic.

The optimal simulation parameters are obtained from the resonant frequency relationship which is written as

$$f_{\mathrm{L}} = \frac{1}{2\pi}\sqrt{\frac{k}{m}} = \frac{e}{2\pi}\sqrt{\frac{Evx}{\rho s^2 l^3}}, \tag{7}$$

where $k = vExe^3/l^3$ and $m = e\rho s^2$, are the elastic coefficient and the PM mass, respectively; ρ, E, x, e, l, s, and v, are the material's density, Young's modulus, elastic beam width, beam thickness, beam length, PM's side, and the sensitive structure's design constant, respectively.

A sinusoidal acceleration with a maximum of 20 g is applied in the vertical direction at the PM center. The FEA result shows that for the optimum parameter values such as $e = 0.3$ mm, $l = 9$ mm, $x = 1.25$ mm, and $s = 4$ mm, the total deformation is uniformly distributed in the PM and has the same propagation profile in the beams (see Fig. 4(b)). As shown in the amplitude–frequency characteristics in Fig. 4(c), the chip vibration fundamental mode shows a maximum amplitude of 30.17 μm and a natural frequency of 8.04 kHz. It has a stable operating state in the range of 120 Hz–2400 Hz. At the resonance frequency, the phase–frequency curve shows a deviation of 180°–0° (see Fig. 4(d)) indicating the diaphragm's resonance state. The simulation results are in agreement with the initial requirements for this diaphragm.

3.3. Chip manufacturing

We adopt the micromachining based on laser processing technology of MEMS for the 6H-SiC WFRSD. This technique has advantages such as good efficiency and flexibility, low thermal reaction, high resolution and usable in OF sensors based on a micro/nano structure cavity.[17,18]

As shown in Fig. 5, the nanosecond ultraviolet laser treatment of the 14.5-mm 6H-SiC wafer is done at a wavelength of 360 nm and under a power of about 5 W. The different treatment steps were performed as follows: (i) scanning at a speed of 1000 mm/s on the SiC element, (ii) creation of wedge-shaped grooves on the surface at each scan, (iii) gradual increase in the depth of the pits, as can be seen in Figs. 5(a)–5(d) of scanning electron microscope. Each laser scan creates a depth of 40 μm, (iv) After a last ultrasound-assisted treatment, the final 6H-SiC element obtained after a total of ten laser scans over a duration of about 5 minutes is illustrated in Fig. 5(e).

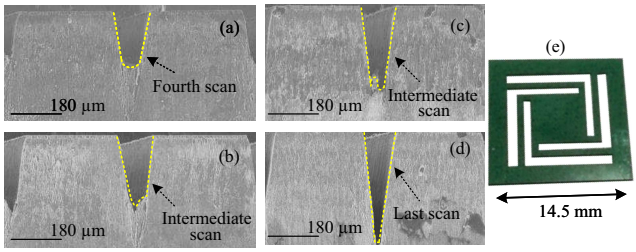


Fig. 5. Scanning electron microscope image of laser processing of 6H-SiC: (a) 4th scan; (b) intermediate "6th" scan; (c) intermediate "8th" scan; (d) last scan; (e) the 6H-SiC sensitive chip.

4. Diaphragm vibration test

For vibration testing, the WFRSD is used as a sensitive element on a fiber optic FP accelerometer probe. The sensing probe cross-section is shown in Fig. 6. The probe packaging mechanism is mainly to fix the designed chip on the ceramic base as shown in Fig. 6(a). Its polished surface is used as a reflecting surface (first mirror) and forms the sensor FP cavity with the OF's end (second mirror). The screw, ceramic tube and adhesive are used in the assembly to immobilize the ceramic core, keep the OF straight and protect it until

the probe exits and glue to make the whole assembly compact, respectively. The integrated sensing probe using the MEMS diaphragm as a vibrating element is shown in Fig. 6(b).

In order to obtain the FP cavity spectral characteristic, the probe is connected to a broadband laser source and an optical spectrum analyzer (YOKOGAWA AQ6370B) via the OF. From the laser source, the light wave is sent into each element via an optical circulator as shown in Fig. 6(c). The probe interference spectrum is visible in the wavelength range of 1475 nm–1596 nm with very low noise level as seen from the spectrum analyzer. These results show that the wide-frequency-range square diaphragm based on 6H-SIC performs very well as the first mirror in the FP cavity.

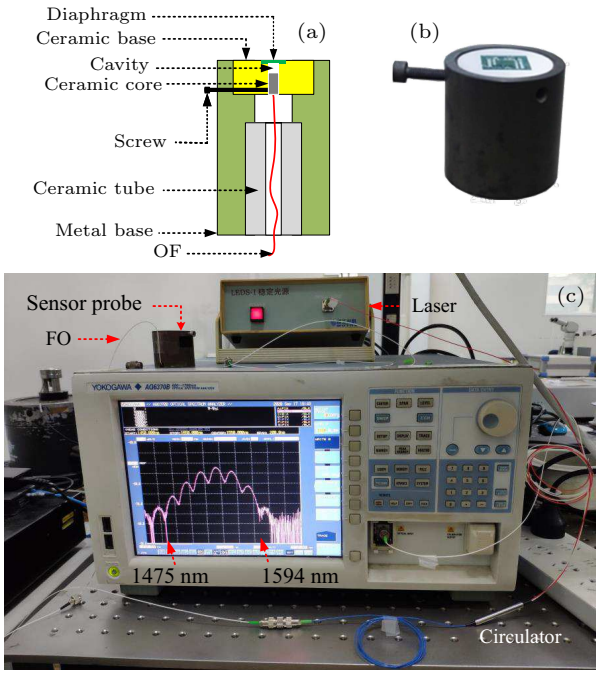


Fig. 6. (a) Fiber optic sensor structural diagram. (b) Sensor's probe. (c) Experimental setup for spectral characteristics.

5. Results and discussion

As can be seen in Fig. 7, the WFRSD test setup is mainly composed of a control PC, laser, demodulation system, power amplifier type 2719, signal generator type 3160-A-042, circulator, vibration exciter type 4808, and the sensor. The sensor is attached to the vibration exciter, it receives the generated and amplified signals from the generator/amplifier block via an electrical cable. At the same time, the laser sends the light wave into the FP cavity via the OF and the optical circulator. Diaphragm vibrations create a shift in the light interference pattern which is sent to the demodulator. The control PC displays the different vibration frequencies detected by the sensor and informs the Q-switching laser of a possible quiescent point (Q-point) readjustment in the working linear area.[19]

The signal demodulation technique chosen for a fiber optic FP accelerometer directly impacts the sensor performance. Intensity demodulation with auto-tracking of the quiescent operating point is adopted in order to perform measurements in real time, and to obtain the desired good performance. The demodulation system used in this work is essentially composed of a control computer, broadband light source, amplifier, a photoelectric detector, and a data acquisition card. The demodulation principle implemented consists in sampling in real time the voltage value resulting from the photoelectric conversion. Thus, when the voltage value deviates from the linear working area, the system automatically adjusts the light source wavelength to ensure that the FP cavity operates again in the linear area. This automatic correction back into the linear area guarantees good measurement performance such as precision, stability, good sensitivity, etc.

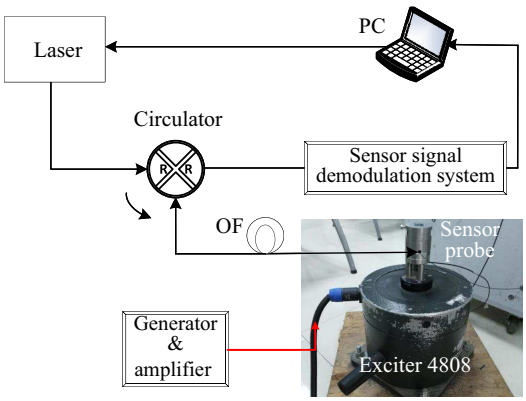


Fig. 7. Experimental setup for WFRSD vibration.

The sensor's amplitude–frequency characteristic is an important dynamic characteristic, which determines the diaphragm response extent to vibration. For characterization tests, the exciter output signal amplitude is set to 0.5 g, the output frequency is gradually increased from 120 Hz to 9500 Hz in steps of 100 Hz and 500 Hz between 120 Hz to 2300 Hz and 2300 Hz to 9500 Hz, respectively. As shown in Fig. 8(a), the amplitude–frequency characteristic curve is relatively smooth in the range of 120 Hz to 2300 Hz, which indicates the wide WFR of the designed chip. Its natural frequency is 7873 Hz, which is lower than that obtained theoretically, and is in line with the initial requirements. This difference is partly due to the fact that in the actual scenario, the diaphragm is fixed and becomes a probe integral part, which impacts its mechanical vibration condition. Under the same excitation conditions, we performed frequency measurements in the frequency range of 120 Hz–2.3 kHz, with a step size of 100 Hz. The WFRSD frequency measurement result is shown in Fig. 8(b). The sensor response shows perfect linearity between the measured frequency and the exciter frequency, with a frequency measurement sensitivity of 0.9995 Hz/Hz. In 120 Hz–1100 Hz, the sensor exhibits a relatively higher relative error (RE) of frequency measurement and is less stable than in 1700 Hz–2300 Hz range (see Fig. 8(c)). The maximum RE over the

working frequency band is 3.75%, and it is 1.15% on average over the whole band. The average RE value in the frequency ranges 120 Hz–1.1 kHz and 1.2 kHz–2.3 kHz is 1.63% and 0.77%, respectively. The high RE observed in 120 kHz–1.1 kHz range is explained by the strong shocks exerted by low frequencies on the chip PM (which is not of dimensions larger than those of the cantilever beams). While for 1.2 kHz–2.3 kHz range, the shocks are faster but of low amplitude, which reduces the measurement error. The designed sensor accuracy is $\text{Abm}/(2300-120)\times 100\% = 0.96\%$ full scale, with Abm = 21.1 Hz, the maximum absolute measurement error.

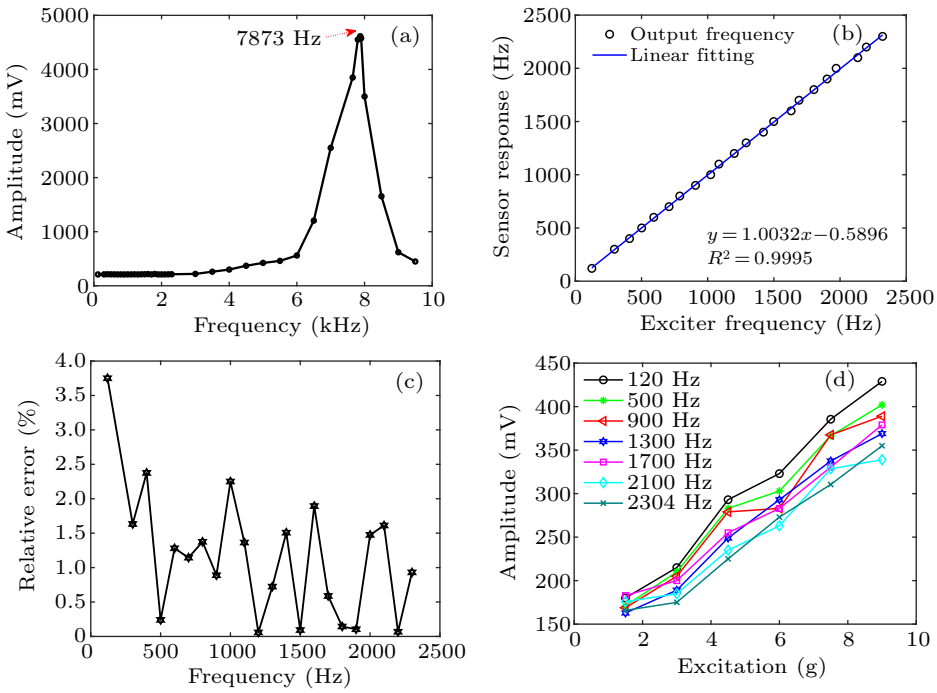


Fig. 8. Graphs of the WFRSD performance: (a) experimental amplitude–frequency characteristic, (b) linear fitting line of the WFRSD response with exciter frequencies, (c) relative error on the frequency measurement, (d) amplitude curves with the acceleration at different frequencies.

Table 1. Comparisons of the designed diaphragms with other reported diaphragms.

Ref.	Diaphragm and beam description	Beam shape illustration	Substrate materials	Diaphragm characterization
[20]	-Square chip -Spiral-beam		SOI	WFR: ≈ 1–160 Hz; NF: 188.5 Hz; sensitivity: no test; linearity: no test.
[14]	*Circular chip *Ring-beam		AlN	WFR: 1–5000 Hz; NF: 7200 Hz; sensitivity: 1.49 mV/g; linearity: ≈ 1; operating temperature: 100 °C.
[21]	-Square chip -4I-beam		4H–SiC	WFR: ≈ 40–600 Hz; NF: 1650 Hz sensitivity: 0.21 mV/g; linearity: 99.8%; frequency measurement error: 0.00587%.
[5]	*Square chip *2G-beam		Si_3N_4 and SiO_2	WFR: ≈ 40–60 Hz; NF: 89 Hz; sensitivity: 183.793 V/g; linearity: 0.99042; operating temperature: no test; resolution: 300 ng.
[19]	-Square chip -4Γ-beam		SiC	Theorical, WFR: 40–500 Hz; NF: Hz; sensitivity 53.7 nm/g; operating temperature: 850 °C.
This work	Triangle chip 3I-beam		6H-SiC	Theorical, WFR: 630–5300 Hz; NF: 44300 Hz; mechanical sensitivity: 0.154 nm/g.
	Square chip 4L-beam		6H-SiC	WFR: 120–2300 Hz; NF: 7873 Hz; sensitivity: 31.5 mV/g; linearity: 0.9995; frequency measurement error: 1.15%; precision: 0,96% F.S.; operating temperature: can reach 850 °C.

Figure 8(d) shows the relationship between acceleration and sensor output voltage for excitation frequency varied from 120 Hz to 2304 Hz; the acceleration excitation is varied from 1.5 g to 9 g for the steps of 400 Hz and 1.5 g, respectively. This characteristic shows that the output voltage increases linearly with the applied acceleration with a linearity of 0.9902, 0.986, 0.9658, 0.9914, 0.98559, 0.9632 and 0.9814 for the frequencies 120 Hz, 500 Hz, 900 Hz, 1300 Hz, 1700 Hz, 2100 Hz, and

2304 Hz, respectively. The sensor's amplitude-acceleration characteristic shows a sensitivity to acceleration measurement at different frequencies 120 Hz, 500 Hz, 900 Hz, 1300 Hz, 1700 Hz, 2100 Hz, and 2304 Hz of 35.6 mV/g, 34.7 mV/g, 30.6 mV/g, 29.1 mV/g, 29 mV/g, 31.8 mV/g, and 30.1 mV/g respectively. These values justify the stability and consistency in vibration of the designed WFRSD. The average sensitivity to acceleration measurement is 31.5 mV/g. The 6H-Sic material can withstand extreme temperatures of 1200 °C,[8] and it has also been reported in our previous work tests at 850 °C.[19]

From Table 1, the sensor using the WFRSD has a wider WFR (120 Hz–2300 Hz) and a higher natural frequency (NF = 7873 Hz) than the reported square chips; it also has a relatively better frequency measurement error, sensitivity, and linearity than most of these sensors. Diaphragms of shapes other than square have a relatively larger WFR and natural frequency. On the other hand, they lose in sensitivity compared to the square diaphragms. The designed triangular diaphragm has better performance among those in its reported category. Compared with other chips of various shapes reported in the literature, the diaphragms proposed in this work have better detection characteristic overall.

6. Conclusion

In this paper, a triangular MEMS chip and a WFRSD all made of 6H-SiC are introduced to solve the acceleration measurement problem with both wide WFR, good sensitivity, and many other good performances. By adopting a triangular structure with an irregular PM shape, the triangular chip has a theoretical sensitivity of 0.154 nm/g, a WFR of 630 Hz–5300 Hz, and a natural frequency of 44.3 kHz. The optimization of structural parameters of WFRSD also enabled a wide WFR of 120 Hz–2300 Hz, an accuracy of 0.96% F.S., a natural frequency of 7873 Hz, and a sensitivity of 31.5 mV/g. Unlike other chips reported in the literature, the proposed ones have solved the difficulties of several good performances of accelerometers at once.

Acknowledgements

Project supported by the National Natural Science Foundation of China (Grant No. 32473216) and Ningbo Youth Science and Technology Innovation Leading Talent Project (Grant No. 2023QL004).

References

[1] Qu Z, Ouyang H, Liu H, Hu C, Tu L C and Zhou Z 2022 *Opt. Lett.* **47** 718
[2] Ahmad N, Ghazilla R A R, Khairi N M and Kasi V 2013 *Int. J. Sign. Proce. Syst.* **1** 256
[3] Beeby S, Ensel G, Kraft M and White N 2004 *MEMS Mechanical Sensors* (Boston: Artech) p. 280
[4] Qu Z, Liu H, Ouyang H, Hu C and Tu L 2020 in 2020 *IEEE Sensors (IEEE,* 2020*)*, pp. 1–4
[5] Zhao M, Jiang K, Bai H, Wang H and Wei X 2020 *Micr. Tech.* **26** 1961
[6] Jiang Y, Li J, Zhou Z, Jiang X and Zhang D 2016 *Sensors* **16** 1660
[7] Afshar B H and Digonnet M J F 2020 *Opt. Lett.* **45** 3933
[8] Huang Y, Tang F, Ma D, Liu Z and Wang X 2019 *IEEE Photon. J.* **11** 1
[9] Lin Q, Chen L, Li S and Wu X 2011 *Meas. Sci. Tech.* **22** 015303
[10] Ran Z, Lu E, Rao Y, Ni M, Peng F and Zeng D 2011 *Proceedings of the* 21*st International Conference on Optical Fiber Sensors*, May 17, 2011, Ottawa, Canada, p. 775318
[11] Waters R L and Aklufi M E 2002 *Appl. Phys. Lett.* **81** 3320
[12] Dirdal C A, Dullo F T, Summanwar A, Tschudi J, Gjessing J and Thrane P C V 2022 *Opt. Lett.* **47** 1049
[13] Li C, Yang B, Zheng X, Guo X, Sun Z, Zhou L and Huang X 2022 *Opt. Lett.* **47** 1883
[14] Chen Z H, Li C Y, Chu S Y, Tsai C C, Wang Y H, Kao H Y, Wei C L, Huang Y H, Hsiao P Y and Liu Y H 2020 *IEEE Trans. Electron. Dev.* **67** 4399
[15] Yang C, Hu B, Lu L, Wang Z, Liu W and Sun C 2022 *Micromachines* **13** 1608
[16] Gilbert J A 1997 *Opt. Eng.* **36** 22
[17] Zhang Z, Gong H, Yu C, Ni K and Zhao C 2022 *Opt. Laser Tech.* **150** 107949
[18] Ran Z L, Liu W J, Liao X, Rao Y J and Chiang K S 2008 *Opt. Express* **16** 2252
[19] Mahissi M, Cai W, Zhang X, Tong X, Zhang C, Ma X and Dossou M 2023 *Opt. Express* **31** 25025
[20] Podder P, Constantinou P, Mallick D, Amann A and Roy S 2017 *J. Micr. Syst.* **26** 539
[21] Zhai Y, Li H, Tao Z, Cao X, Yang C, Che Z and Xu T 2022 *Micr. Eng.* **260** 111793